



HAL
open science

On the Divergence Mechanisms Analysis of a Vibrating Blade Subjected to Repetitive Rubs With an Abradable Coating

Fabien Goldspiegel, Gerald Portemont, Julien Berthe

► **To cite this version:**

Fabien Goldspiegel, Gerald Portemont, Julien Berthe. On the Divergence Mechanisms Analysis of a Vibrating Blade Subjected to Repetitive Rubs With an Abradable Coating. *Journal of Turbomachinery*, 2022, 144 (5), 10.1115/1.4053018 . hal-03833825

HAL Id: hal-03833825

<https://hal.science/hal-03833825>

Submitted on 24 Mar 2023

HAL is a multi-disciplinary open access archive for the deposit and dissemination of scientific research documents, whether they are published or not. The documents may come from teaching and research institutions in France or abroad, or from public or private research centers.

L'archive ouverte pluridisciplinaire **HAL**, est destinée au dépôt et à la diffusion de documents scientifiques de niveau recherche, publiés ou non, émanant des établissements d'enseignement et de recherche français ou étrangers, des laboratoires publics ou privés.



Distributed under a Creative Commons Attribution - NonCommercial 4.0 International License

On the Divergence Mechanisms Analysis of a Vibrating Blade Subjected to Repetitive Rubs With an Abradable Coating

F. Goldspiegel, ONERA/DMAS, F-59014 Lille, France e-mail: fabien.goldspiegel@protonmail.com

G. Portemont, ONERA/DMAS, F-59014 Lille, France e-mail: gerald.portemont@onera.fr

J. Berthe, Univ. Lille, CNRS, Centrale Lille, UMR 9013 - LaMcube - Laboratoire de Mécanique, Multiphysique, Multi-échelle, F-59000 Lille, France, e-mail: julien.berthe@onera.fr

Aeronautical compressor fans, currently, operate with minimal blade–casing clearance. Therefore, this makes the occurrence of rub events very likely. Under specific circumstances, the blade undergoes excessive amplification of contact-induced oscillations, called hereafter divergence, which can be critical for the structural integrity of the engine. This article proposes an investigation of the mechanisms responsible for the blade divergence. Experiments are conducted on a fully instrumented laboratory setup, consisting of a single flat blade being moved toward a rotating cylinder to initiate interactions, while monitoring the vibrations and the evolution of wear on the abradable coating. Two synchronization mechanisms have been identified as facilitating the divergence: (i) the inherent setup synchronization between the vibration modes related to the horizontal and vertical motion of the blade; (ii) the preferential blade–coating interactions in the vicinity of periodically distributed irregularities of the abradable coating, which act as a source of excitation of the vibrations.

Keywords: blade–casing interaction, rubbing, abradable coating, modal interaction, fan, compressor, and turbine aerodynamic design, turbine blade and measurement advancements

1 Introduction

1.1 General Context. Nowadays, the engineering of aircraft turbomachinery is oriented toward two main targets: (i) extended flight range capacity and (ii) minimized fuel consumption. Both targets can be merged into a global concern for enhanced engine efficiency. To satisfy these objectives, structural as well as aerodynamical optimization paths are considered with lighter and stiffer materials or higher engine operating temperatures and pressures. Minimizing the in-service blade–casing clearance at the compressor stages has been stated by Benini [1] to significantly influence the efficiency of aeronautical compressors. However, this tends to increase the probability of in-service interaction events between the blade and the casing. Therefore, engineers and researchers are challenged to ensure the structural integrity of the engine across its full operating range, taking into account the possibility of blade–casing interactions. Engines must be protected from a regime of rotor instability [2] in which vibration-induced fatigue failure of rotor blades can occur. It has been observed that, after a blade loss, subsequent rotor unbalance and debris ingestion can cause a chain reaction, which tends to exacerbate engine damage through the higher vibrational amplitude of the rotor parts [3]. Several authors have reported incidents initiated by such blade damage [4] and activated by one of the following mechanisms: (i) impact of sand or snow [5] or (ii) a coupled effect of corrosion pits with the vibration-induced fatigue of the blade under natural frequencies [6,7]. It has been shown in the works of Witek et al. [8], with the help of finite element simulations, that the blade exhibits higher stress levels under vibration at the second natural frequency than within the regular dynamic loading conditions, which therefore promotes a greater likelihood of crack initiation in the vicinity of the corrosion pit than anywhere else in the blade.

The blade vibrations can be dangerous, but they are inherent to the engine dynamics and are driven by mechanisms that can be split into two main categories: (i) aeroelastic instabilities, known as flutter, and related to unsteady airflow impacting the blade, and (ii) mechanical instabilities, characterized by any source of excitation causing blade resonant vibration, i.e., a number of blade oscillations, which is a multiple of the rotation speed [2].

1.2 Blade–Casing Interactions. Except in the situation of an excessively unbalanced rotor, the blade vibrations deriving from mechanical instabilities are mostly related in the literature to forced responses due to blade–casing rubbing [9]. Blade expansion under centrifugal loads, rotor–stator differential thermal dilatation, high vibration level of rotor parts, and synchronization between blade and casing vibration modes are some of the most commonly cited phenomena for promoting blade–casing contact [10]. While the first rub can be initiated by any one of these phenomena, it can be sustained by several others, with constantly changing contact conditions at the interface. Based on simulations, Millecamps [11] gave an overview on how contact conditions evolve, at the compressor stage of a turbomachine, from the competition between two kinds of mechanisms: on the one hand, the rub-induced heat tends to expand the blade, which reduces clearance and promotes contact; on the other hand, as the abradable coating gets thinner, the casing temperature increases and ovalization is intensified, which in turn has the effect of increasing the clearance. One mechanism closes the gap, while the other opens it. This is an example of the highly coupled nature of blade–casing interactions, requiring continued investigation through combined experimental–numerical approaches to attain greater insight into these mechanisms.

1.3 Rub-Induced Blade Oscillations. The experiments conducted by Padova et al. [12] on a single-bladed disk forced to rub against a metal casing have confirmed that the blade vibrates after rubbing, and these oscillations are amplified between the successive

rubs. The force components allocated to the blade tip also exhibited significant changes between the rubs, with the tangential component increasing while the axial one decreased through the successive rubs. An oscillatory wear pattern was also observed on the casing, which was consistent with the torsional excitation of the blade during incursion. Further experiments of Millecamps et al. [13] on full-scale turbomachinery have reinforced the assumption of a coupling between the casing wear and the blade vibration throughout the test. It was pointed out that the post mortem wear pattern is in perfect agreement with the blade natural frequency: seven oscillations per revolution facing seven prominent wear lobes on the casing. Furthermore, this configuration brought the blade, in the last stage of these experiments, into a critical divergent behavior, which culminated in blade failure. So far, no conclusions could be drawn on which mechanism is responsible for the repetitive rubs, which lead to blade divergence. But the works of Legrand et al. [14] later tackled this question using simulations of blade–casing interactions. It was observed that (i) the largest blade vibration amplitudes are obtained at rotation velocities/frequencies, which complied with the K th harmonics of the blade’s natural frequencies ($K \in \mathbb{N}$) and (ii) the vibrations at these velocities are associated with a contact-induced wear pattern made up of K distinct lobes. Williams [15] ran equivalent simulations, but he associated the occurrence of blade divergence with the constant increase of rotor velocity: the blade motion is amplified as it always contacts virgin coating material; the rubbing reaction increases proportionally with amplitude, which once again tends to sustain divergent blade behavior. Another phenomenon that can influence divergent behavior has been proposed by Sinha [16] as a logical inference of a Timoshenko blade subjected to rotation. It was stated that, for a rotating beam only, an energy transfer mechanism between the flexural and axial vibration modes exists due to the Coriolis effect, which feeds the lateral deflection of the blade via axial impulse. In addition to all these phenomena affecting every rotor blade separately, the relative motion of the bladed-disk with the casing must also be considered from a structural viewpoint to assess the probability of occurrence of a rub event.

1.4 Modal Interaction. Initially considered rigid with a pre-distorted geometry, the casing’s vibrations are in fact nonnegligible, just as for the bladed-disk. These vibrations are propagated in both structures, according to the direction of rotor rotation, in a forward direction for the bladed-disk and in the opposite direction for the casing [17]. Resulting from this consideration is the existence of a critical condition of interaction between the two structures, occurring at a given rotation velocity, for which both traveling wave speeds would be coincident. These structures would be consequently forced into resonance by their repetitive interactions and a very large amplitude of vibrations would be experienced. Legrand et al. [18] investigated this phenomenon considering different configurations of interactions involving a rotor consisting of N periodically distributed blades and a stator/casing with K -nodal diameters. It appeared that divergent behavior was

promoted for the casing and the bladed-disk, close to critical rotation velocity [10], when the ratio N/K is not an integer: the contact locations are not equally distributed on the casing perimeter and move from blade to blade over time; both the casing and the bladed-disk are dynamically deformed and excited by intermittent contacts, which occur on a regular basis due to a symmetrical pattern of contact locations on the casing. This promotes a counter-rotating mode in the rotor and a forward-rotating mode in the stator and maintains the vibration amplification for both structures.

Any phenomenon likely to close the blade–casing clearance is of major interest. Most of these phenomena have been already studied, at least partially. But the dynamics of blade–casing interaction during the establishment of blade divergent behavior remains widely misunderstood. Even the more advanced simulations [19] are not currently able to explain every occurrence of blade divergent behavior in complex rotor–stator configurations. Although it is very unlikely due to access and rotating instrumentation issues, experiments run on a full-scale turbomachinery would involve so many phenomena that it would be very complex to pick out one in particular and determine its effect on the initiation of blade divergence. These considerations convinced the authors that new blade–casing experiments on a laboratory setup could be appreciated by both engineers and researchers of the community and would be likely to provide relevant insight into the actual mechanism of blade–coating coupling. The investigations proposed in what follows attempt to expose the circumstances under which blade divergent behavior appears and to estimate the importance of the role of coating wear evolution in the mechanism suspected to sustain blade divergence.

2 Experiments

The approach chosen in this article consists of a drastically simplified configuration of blade–coating interactions, setup, and blade geometry, to enable accurate monitoring of blade oscillations and rub events. Two experiments are investigated here to present in the simplest form the two underlying mechanisms that are involved in the occurrence of blade divergence.

2.1 Setup. The present setup was developed at ONERA, the French Aerospace Lab, and presented in the works of Baiz et al. [20] and later Mandard et al. [21]. Its main feature consists in the fact that the abradable coating is subjected to rotation, whereas the blade is laid on a separate frame, which be translated toward the coating. The setup is depicted in Fig. 1 with its main components and instruments in a schematic form to avoid unnecessary technical considerations. Readers interested in additional depictions of the setup should refer to the works of Mandard et al. [22].

The abradable coating is an AlSi-Polyester solid powder (Rockwell harness HR15Y = 46) sprayed over a 300 mm-diameter aluminum cylinder, which can rotate up to a relative blade–coating velocity of $V_T = 100$ m/s. The blade has a parallelepipedal shape

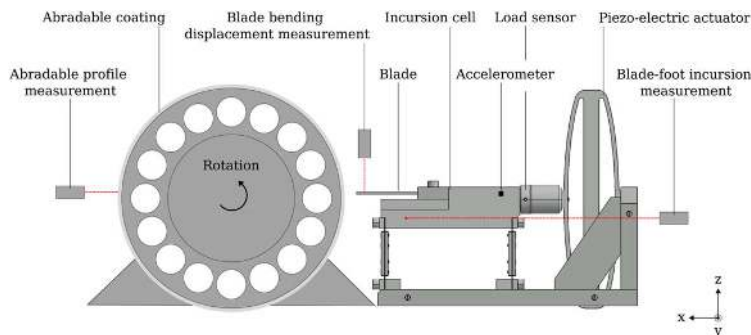


Fig. 1 Blade–coating interaction setup and its main instruments

with length, width, and thickness, respectively, set to $L = 62$ mm, $W = 15$ mm, and $T = 2$ mm. It is made of titanium alloy (TA6V) and fixed on a rigid unit, called an incursion cell hereafter, and connected to an amplified piezoelectric actuator (APA 750 XL). An electric pulse initiates its motion to fill the gap with the abrasible coating and therefore generate in a few milliseconds an incursion in the range $[0; 100 \mu\text{m}]$.

Both blade and setup designs have been chosen to appropriately address the blade–casing interactions occurring in a turbofan as simply as possible. Within this setup, the actual relative blade–coating velocities encountered in a turbofan could not be reached, but we assume that the global kinematics of blade–coating interactions is adequate since the natural bending frequencies and dynamic stiffness of the simplified blade are similar to those of the compressor blades; the length and cross section have been adjusted to reflect actual blade stiffening under centrifugal load. An additional difference between a real turbofan and the setup configuration consists in the geometrical conditions of contact between the abrasible coating and the blade. Since the abrasible coating has been sprayed over a cylinder, it has a reversal curvature vis-a-vis its situation in the casing of an actual turbofan. However, the two radii of curvature are the same order of magnitude (several hundred millimeters) and the reversal curvature is not expected to change the contact conditions between the blade and the abrasible coating.

Despite all these differences, the setup concept is very convenient since it enables accurate control and measurement of blade motion throughout the interaction stage. The incursion cell, the abrasible coating, and the blade are instrumented to fully capture the dynamics of blade–coating interactions. The different measurements are listed in the following key points:

- Φ (deg): abrasible coating angular position, in the angular cylinder’s frame, which passes through the interaction zone.
- V_e (V): electric pulse sent to the actuator.
- D_N (μm): incursion cell horizontal displacement (i.e., blade foot apparent incursion).
- D_T (mm): blade bending displacement at the distance from clamp $x = L - 17.5$ mm.
- w (μm): relative coating profile.
- a_N (m/s^2): blade foot acceleration.
- f_s (N): incursion force.

Thus, a typical blade–coating interaction test consists of a sequence of six main operations:

- (1) The electric motor reaches its operating speed. The relative blade–coating velocity V_T is set.
- (2) An electric pulse V_e is sent to the actuator, which implies the radial stretching of the oval shell.
- (3) The incursion cell connected to the actuator is translated toward the rotating cylinder with an apparent incursion D_N and acceleration a_N .
- (4) When blade–coating initial clearance D_{N0} is reached, contact occurs. An incursion force f_s is recorded and the blade tip is moved up toward the imposed rotating motion.
- (5) The blade and the incursion cell alike undergo contact-induced oscillations, which are respectively captured as blade bending displacement D_T and incursion cell displacement D_N .
- (6) As the cylinder is spinning, a laser displacement sensor measures the surface state of the cylinder’s track. These profiles can be compared per successive revolution and the changes assigned to the wear mechanisms occurring due to blade–coating interactions. Hence, for every cylinder revolution, a wear map is computed, and it depicts the current coating profile according to the abrasible angular position Φ on the cylinder, written hereafter $w(\Phi)$.

2.2 Measurement System. The test duration is very short (0.5–1 s) and requires a high-frequency acquisition system. A Dewetron 5000 was chosen to collect data from every sensor

perfectly synchronized at 1 MHz. The apparent incursion D_N , the blade bending displacement D_T , and the relative coating profile w are measured using laser displacement sensors, respectively, two Keyence LC2450 and one Keyence LK-H082. The acceleration a_N is obtained averaging signals from two B&K 4344 accelerometers located on both sides of the incursion cell. The incursion force f_s is measured with a Kistler 9031A piezoelectric load sensor tight between the incursion cell and the actuator. An encoder embedded in the brushless motor provides the cylinder angular position Φ . In addition to these instruments, a Photron Fastcam SA-X high-speed camera is placed beside the setup and it records interaction, debris, and induced blade oscillations at 12,500 frames per second with a resolution of 1024×1024 pixels. These images enable the identification of contact scenarios and mechanisms of incursion accommodation as discussed in Refs. [21,22], but they will not be used here since they are not relevant to the topic we have chosen to discuss in the present article.

2.3 Abradable Coating Profile. As depicted in Fig. 1, the present setup enables an in situ measurement of the coating profile w . A laser displacement sensor records the coating profile of the cylinder 180 deg before it is brought into the interaction area. This allows the allocation of the coating profile series to be corrected to coincide with the time it reaches the interaction area.

2.4 Initial Blade–Coating Clearance. In practice, coating is set manually on the setup, moving the incursion cell along the x -axis until a predefined value is reached. Therefore, a rub event is expected to be identical all along the blade width when the initial clearance, written D_{N0}^{theo} , is fulfilled. Yet, this is only theoretical, and the remaining play in the mechanism or tolerances in the blade geometry will induce a rub event when a slightly different clearance is considered: the effective clearance D_{N0}^{eff} . These values have been chosen in the experiments according to the first variation of the blade vertical position and are presented in Table 1.

2.5 Experimental Conditions. In this article, we have chosen to focus on two blade–coating interaction experiments of detailed in Table 1 : the first consists in a single rub, set by actuator, and followed by several unwanted rubs; the second involves numerous repetitive rubs leading to blade divergence. These tests were run at ambient temperature.

Test 1 was initiated using a 70 V triangle shaped pulse V_e sent to the actuator. It induced an apparent incursion variation of the blade $pN0 = 149 \mu\text{m}$ and a first interaction.

However the test 2 initiation did not require any electric pulse to be sent to the actuator. A steady electric signal V_e was selected to turn the blade–coating clearance to zero ($pN0 = D_{N0}^{eff} = 80$). The incursion cell’s oscillation was then slightly and gradually amplified through micro-contacts until an effective rub was noticed with a significant modification of the blade foot apparent incursion D_N and blade bending displacement D_T .

2.6 Global Kinematics of Experiments. A global overview of these experiments is depicted in Figs. 2 and 3 where horizontal

Table 1 Conditions of experiments

# (–)	V_T (m/s)	D_{N0}^{theo} (μm)	D_{N0}^{eff} (μm)	$pN0$ (μm)	Interaction (–)
1	92	100	118	149	Multiple rubs
2	50	0.0	80	80	Divergence

Note: D_{N0}^{theo} , theoretical initial blade–coating clearance; D_{N0}^{eff} , effective initial blade–coating clearance; $pN0$, electric pulse-induced apparent incursion; δ_0 , initial pulse-induced effective incursion; δ_0 , $pN0 - D_{N0}^{eff}$

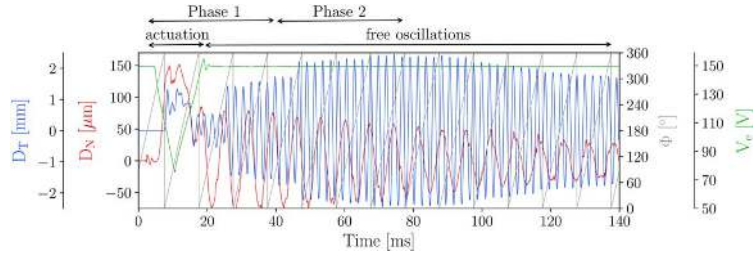


Fig. 2 Overview of blade-coating kinematics in experiment 1. Note: Two phases of interests: phase 1 for $t \in \sim[0; 40 \text{ ms}]$ and phase 2 for $t \in [40; 80 \text{ ms}]$.

blade foot motion D_N , vertical blade bending motion D_T , and electric voltage sent to the actuator V_e are plotted according to time and coating angular position Φ .

For the sake of readability, it should be noted that Figs. 2 and 3 are not plotted on the same y -scale range since displacements recorded in experiment 2 are at least twice as large as those recorded in experiment 1.

In experiment 1, the actuation induced a direct blade-coating contact, which is clearly identified at $t_1 = 8 \text{ ms}$ —when initial clearance reached zero ($D_N = D_{N0}^{eff}$)—by simultaneous variation of both horizontal and vertical blade displacement amplitudes (see Fig. 2). Thus, the blade bending displacement is maintained throughout the contact until $t_2 = 15 \text{ ms}$ when the actuation involved in a backward motion restores a positive blade-coating clearance ($D_N < D_{N0}^{eff}$). The blade is then back at the equilibrium position, far from contact, but it keeps oscillating horizontally as well as vertically. Blade bending displacement amplitude (D_T) keeps increasing until a maximum is reached at $t_3 = 74 \text{ ms}$, followed by a decrease. This shows that several contacts have occurred during the free oscillation stage leading to an uncontrolled amplification of the blade bending displacement.

In experiment 2, the electric signal sent to the actuator is almost constant at $V_e = 56 \text{ V}$. Only a slight variation of voltage can be noted at time $t \in [240; 300] \text{ ms}$, which can be explained by the variation of the piezoelectric stacks' electric potential when subjected to intense loads. Unlike in experiment 1, blade-coating contact is not initiated deliberately. The incursion cell starts to oscillate horizontally without any significant variation of the blade bending displacement up to $t_1 = 190 \text{ ms}$. Then both horizontal and vertical displacements undergo, after four cylinder revolutions ($t_2 = 270 \text{ ms}$), a critical amplitude variation of, respectively, $\pm 300 \mu\text{m}$ and $\pm 8 \text{ mm}$. Finally, both amplitudes decreased gradually until $t_3 = 550 \text{ ms}$, when the blade bending variation became negligible.

It should be noted that, for convenience, several phases of interest have been identified in both experiments. These is shown in Figs. 2 and 3, and they will be useful when the sequence of events and the underlying mechanism of oscillation amplification is investigated.

2.7 Blade-Incursion Cell Vibrational System. The diagrams discussed in Sec. 2.6 have shown that blade and incursion cell state of motion can be twofold: either it is driven by contact with the abradable coating, therefore it oscillates according to rub event frequency, or it is out of any contact occurrence in a state of free oscillation. This observation is valid not only on this laboratory setup but can also be extended to the full-scale turbomachinery configuration in which blade and casing have their own natural frequencies.

The equivalence of this setup with a turbofan vibrational system can be questioned when considering their respective degrees-of-freedom regarding the conditions of blade-coating contact. In a full-scale turbofan, the clearance is filled—promoting contact—by (i) bladed-disk radial displacement, (ii) casing radial displacement, (iii) coating geometry (local thickness), and (iv) blade vibration state (relative distance to static equilibrium). The centrifugal-based and heat-induced mechanisms can also be considered in the closing clearance but are related to larger time-scale than experienced by vibration-based phenomena [23]. Since we assume that the blade motion runaway initiation is more likely attributable to short time-scale phenomena, it can be legitimately limited for the moment to these four parameters. The bladed-disk motion of an actual turbofan can be compared to the horizontal incursion cell motion of our setup. The roles of blade vibration and coating geometry are equivalent in both setup and turbofan configurations. However, the casing radial motion is not taken into account in the setup: the cylinder is assumed to be rigid and properly balanced. This means that only actual turbofan configurations in which the casing or the bladed-disk vibration is negligible, or subject to identical vibration, can be replicated by the current setup since bladed-disk and casing are in a steady state with no relative motion.

The contact conditions should be similar in both configurations and comply with one of the three main types of contacts defined by Legrand et al. [18]: permanent, intermittent, and blocked. In the regime of intermittent contact, the blade contact has a short duration, disappears, and is followed by a new contact. Therefore, it is assumed that a coincidence between the vibrational modes of the blade and casing, and the rotor speed of rotation might

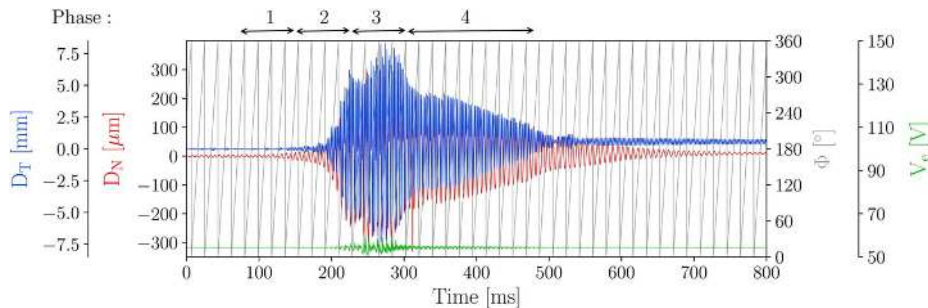


Fig. 3 Overview of blade-coating kinematics in experiment 2. Note: Four phases of interests: phase 1 for $t \in [80; 154 \text{ ms}]$, phase 2 for $t \in [154; 228 \text{ ms}]$, phase 3 for $t \in [228; 302 \text{ ms}]$, and phase 4 for $t \in [302; 468 \text{ ms}]$.

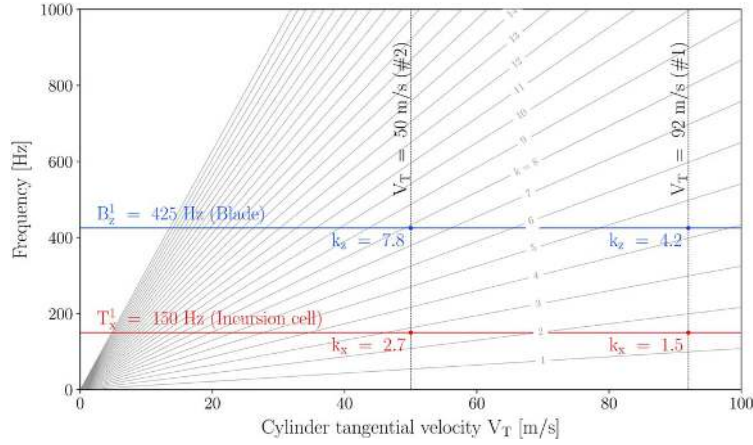


Fig. 4 Campbell diagram of the {blade–incursion cell} vibrational system in experiment 1 and 2. Note 1: B_z^1 and T_x^1 are, respectively, the first blade bending and incursion cell translation natural frequencies. Note 2: Gray lines are vibration-order regime related to term k (oscillations per cylinder revolution).

induce, after the first contact has been initiated, a situation of modal interaction [10]. To investigate these states, the “Campbell diagram” is generally appreciated by authors of the rotordynamics community. It has been used in the works on Refs. [24–26] to study the effects of blade tip–casing interactions and depicts in a very intuitive way the vibration system at different rotor–stator relative velocities. Since an analogy has been formulated between the setup and a real turbofan configuration, based on the consideration of their respective degrees-of-freedom, we have assumed that an extension of the use of a Campbell diagram applied to the setup configuration would be relevant to describe the vibration states of the blade and the incursion cell at different blade–coating relative velocities in the experimental conditions.

This diagram is shown in Fig. 4 with the appropriate setup features and as applied to the conditions of our experiments. Gray lines are the vibration-order lines, referring to the engine-order lines of turbomachines, and associated with the term k , which, for instance where $k=6$, describes how the frequency evolves with the cylinder tangential velocity to maintain six oscillations per cylinder revolution. Horizontal blue and red lines relate, respectively, to the first blade bending natural frequency $B_z^1 = 425$ Hz and the first incursion cell translation natural frequency $T_x^1 = 150$ Hz. Both of these frequencies have been computed using Fourier analysis applied to the displacement signals (D_N , D_T) under free oscillation. Intersections between the frequency-related lines and the vertical lines indicate how many oscillations must be observed for the blade and the incursion cell at every cylinder revolution in experiment 1 and 2 when no contact occurs with the abradable coating. It reveals that, for every horizontal oscillation of the incursion cell, the blade oscillates vertically n_k -times with $n_k = B_z^1/T_x^1 \approx 2.8$.

3 Blade–Coating Interactions

From the consideration of the previous diagrams only, the understanding of rub events is limited because it involves time series, which do not properly reveal the evolution of contact location, their distribution on the coating, and their consequences on the rub-induced wear and the blade dynamics. To overcome this issue, we proposed to switch the reference framework of our study from time to cylinder revolution. This makes it easier to capture and track contact occurrence throughout the tests.

3.1 Evolution of Coating Profile. Using measurements obtained before and after the blade–coating interaction occurred

in both experiment 1 and 2, the initial and final profiles were computed. Figures 5 and 6 show that a mean coating profile line was extracted from data obtained after a large number of cylinder revolutions and then compared to highlight the angular location of coating loss or addition induced by the rubs. Furthermore, it can be noted that the errorbars related to the mean curves are small in terms of the amplitude of the curves, which attests to the consistency of the present method in properly approximating the coating profile.

3.2 Interaction Analysis—Experiment 1. Three variables were previously introduced as indicators of the blade–coating

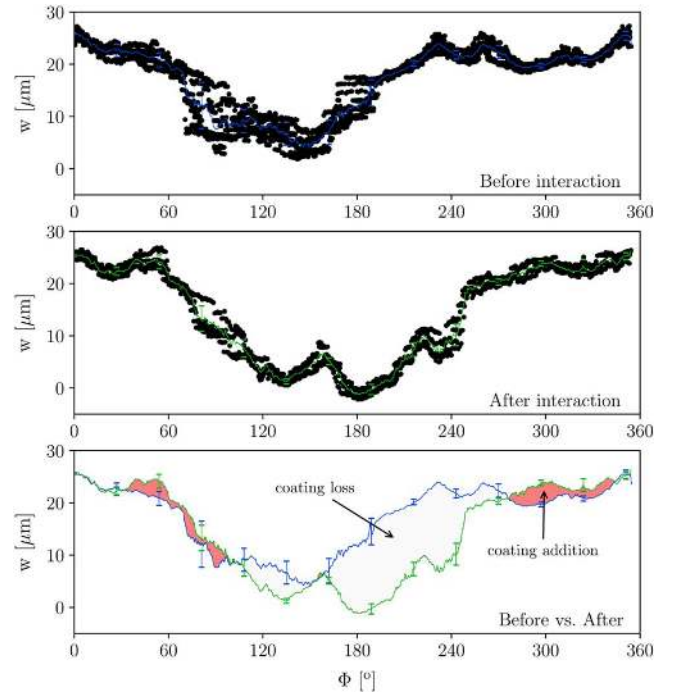


Fig. 5 Coating profile before interaction (top), after interaction (center), and comparison before versus after interaction (bottom) in experiment 1. Note 1: Black dots are raw data obtained over 9 and 4 cylinder revolutions, respectively, before and after interaction. Note 2: Blue and green lines are the mean profile lines.

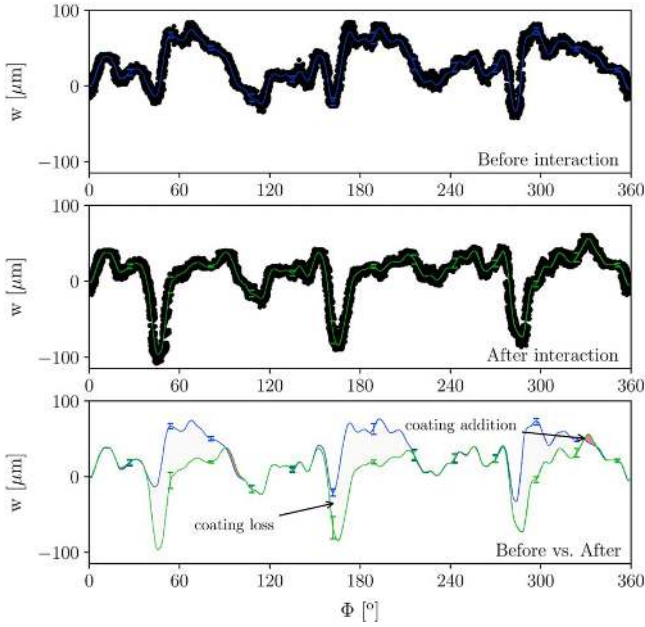


Fig. 6 Coating profile before interaction (top), after interaction (center), and comparison before versus after interaction (bottom) in experiment 2. Note 1: Black dots are raw data obtained over 78 and 135 cylinder revolutions, respectively, before and after interaction. Note 2: Blue and green lines are the mean profile lines.

interactions: the blade foot apparent incursion (D_N), the blade bending displacement at 17.5 mm from the tip (D_T), and the abrable coating profile (w). These ones have been incorporated into a common chart to build a global interaction diagram with the coating angular position (Φ) as the reference axis. It is applied to experiment 1 – phase 1 in Fig. 7(a) and describes the evolution of these variables over four cylinder revolutions. The same color code is used for the three diagrams: each color is assigned to a full revolution. The initial and final average coating profiles presented in Figs. 5 and 6, respectively, represented on this diagram by a thick and a thin black line, are used to highlight under which boundaries the coating profile moves throughout the revolution, in situ coating profile data are compared revolution-by-revolution and a color patch is drawn with respect to the wear location and the thickness loss. It should be noted that these data are not as accurate as the averaged initial and final profile lines stated earlier; hence, it might locally exceed the boundaries.

Phase 1. In the particular case of Fig. 7(a), associated with experiment 1 – phase 1, it can be noted that revolutions start from initial angle $\Phi_0 = 88$ deg and move in the direction of rotation (to the right). The first contact is observed at approximately $\Phi^{(\text{Rev}1)} = 5$ deg with a positive incursion inside the abrable layer followed by a significant amplification of the blade tip vertical position. The actuation is maintained until $\Phi^{(\text{Rev}2)} = 300$ deg, in the second revolution, when blade vertical position returns to its initial position ($D_T = 0$). During actuation, the blade oscillation is limited and follows the coating profile contour. A noteworthy coating loss is observed in the region $\Phi = [165; 250]$ deg and fills almost the whole area between initial and final coating profile lines. Few color patches can be noticed elsewhere, in further revolutions, but they relate to smaller coating profile variations than those observed during actuation. From the middle of the second revolution to the end of the fourth revolution especially—when actuation ended and the incursion cell has moved back to its initial position—the coating loss is barely visible. Indeed no significant wear can be

observed and the blade starts free oscillations with a characteristic number of oscillations per revolution $k_z = 4.2$ (see Fig. 4). However, it cannot be considered to be in a purely free oscillation stage, since blade vertical displacement (D_T) undergoes significant amplitude increases in the third and fourth revolutions, indicating that several rub events have occurred. The evolution of blade foot apparent incursion (D_N) somewhat explains this issue: After actuation, the blade and incursion cell alike enter a free oscillation regime with the following number of oscillations per revolution: $k_z = 4.2$ (blade) and $k_x = 1.5$ (incursion cell). This is confirmed with a typical three-lobe D_N profile, which pops out every two revolutions, considering the set of revolution 3 (–) and 4 (–). Thus, it can be noted that, in the third and fourth revolutions, a coincidence exists between the maximum of the incursion cell position towards the x -axis and the sudden increase of the blade tip position toward the z -axis. The incursion cell motion is therefore synchronized with the blade motion and induces, in the last two revolutions of phase 1, three contacts, which keep increasing blade tip amplitude up to its maximum, $D_T = 1.7$ mm at $\Phi^{(\text{Rev}4)} = 80$ deg.

Phase 2. The blade–coating interaction diagram of this phase is presented in Fig. 7(b) and focuses on the four revolutions following phase 1. The actuation has been stopped for a while, but the amplitude of blade vertical displacement reaches a higher value than experienced before. A possible explanation would be to infer a transfer mechanism, which occurred due to incursion, moving abrable material from the cylinder to the blade tip. An overlength of about 50 μm would be consistent with the repetition of contact despite a positive clearance.

The same oscillation pattern— $k_z = 4.2$ (blade) and $k_x = 1.5$ (incursion cell)—is encountered in these revolutions for D_T and D_N as for those of phase 1. This suggests that blade–coating contacts should proceed at the same rate: three contacts every two revolutions. However, the effectiveness of a rub can be confirmed only if it is coincident with a variation of blade tip amplitude. The sequence of events is analyzed and a total of five rubs are counted, and their subsequent blade vertical positions are measured, written $D_T^{(i)}$ for the i th rub. The following values have been extracted from the diagram: $D_T^{(1)} = 2.2$ mm, $D_T^{(2)} = 2.25$ mm, $D_T^{(3)} = 2.29$ mm, $D_T^{(4)} = 2.43$ mm, and $D_T^{(5)} = 2.46$ mm. It appears that amplitude keeps increasing until a global maximum is reached at $\Phi^{(\text{Rev}4)} = 248$ deg. Beyond this time, blade motion is slowly damped, as can be noted from the consideration of global kinematics in Fig. 2.

As a matter of fact, the fifth touch results in the last situation where the following two conditions were satisfied: (i) a positive D_N and (ii) a close-to-zero D_T . These conditions of “contact occurrence” were met for experiment 1 as a whole once actuation ended and a phase shift was set between the incursion cell oscillation and the blade vertical oscillation. Rubs frequency was maintained as long as these conditions were satisfied and the desynchronization between both horizontal and vertical motion was preserved. Yet after the global maximum of the blade vertical position was reached—after the fifth touch at $\Phi^{(\text{Rev}4)} = 248$ deg—the incursion cell caught up with the blade motion. A new synchronization regime is then set, which, in addition to the damping of incursion cell displacement, tends to prevent contact occurrence: the blade tip reaches its maximum bending when the blade foot/incursion cell is fully translated toward the abrable coating.

3.3 Interaction Analysis—Experiment 2. The conditions of experiment 2 were introduced in Table 1 and Fig. 4. No real actuation was deliberately initiated; the absence of blade–coating initial clearance promoted micro-contacts well before phase 1 started (see Fig. 3) and induced the progressive excitation of the incursion cell. However, these oscillations became significant in phase 1 only when blade oscillation experienced an increase of amplitude over four cylinder revolutions.

The same method of investigation as for experiment 1 is continued here, and blade–coating interactions are tracked according to

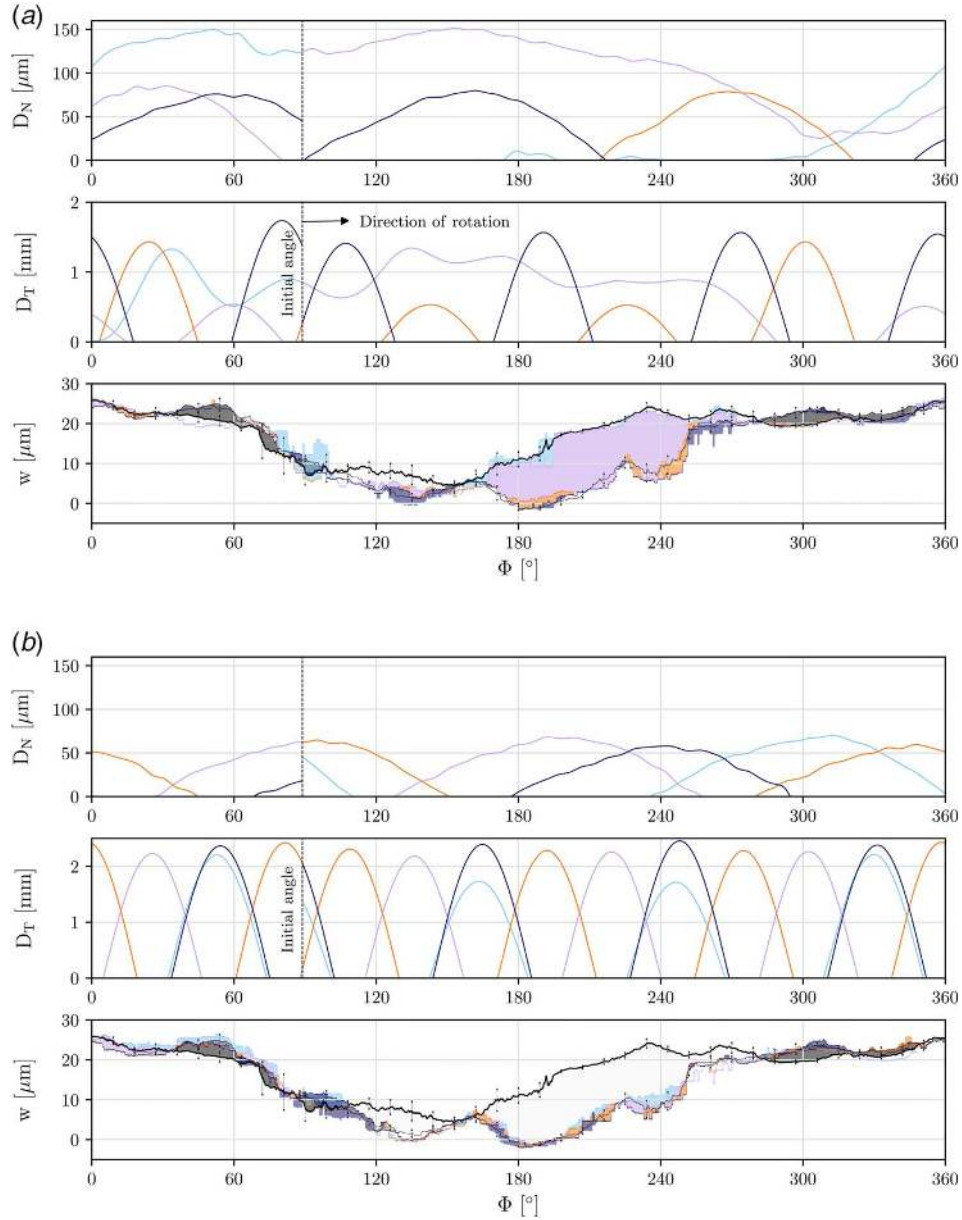


Fig. 7 Blade-coating rubs diagrams of experiment 1 in (a) phase 1 and (b) phase 2. Note 1: Colors are set to cylinder revolution: Revolution 1 (–), 2 (–), 3 (–), and 4 (–). Note 2: Three embedded diagrams are plotted according to the coating angular position Φ : blade foot horizontal displacement D_N , blade bending vertical displacement D_T , and coating profile w and the coating loss.

the frame of the abradable coating position (Φ). Cylinder velocity is set to $V_T = 50$ m/s, which moves, in this experiment 2, the number of expected free oscillations per revolution to $k_z = 7.8$ (blade) and $k_x = 2.7$ (incursion cell).

Phase 1. The blade-coating interaction diagram is presented in Fig. 8(a) and focuses on four revolutions. In phase 1, the emergence of an oscillation pattern is noted in the curves of the blade vertical position (D_T) and blade foot horizontal position (D_N). The blade vertical position oscillates according to its natural frequency with a 45 deg period, which is consistent with the characteristic number $k_z = 7.8$. This motion is interrupted at $\Phi^{(\text{Rev}1)} = 40$ deg by a possible touch and the blade oscillation curve (D_T) is significantly flattened. In the second revolution, the oscillation pattern is disrupted once again at the coating angular position $\Phi^{(\text{Rev}2)} = 165$ deg and $\Phi^{(\text{Rev}2)} = 280$ deg. An explanation of contacts promoted at these same locations could be the coincidence of a sudden

variation in the blade motion and a significant change in the coating profile (w).

Before the first contact occurred, it can be noted that the average coating profile is in the range $w = [-30; 76]$ μm , locally reaching $w(\Phi = 172 \text{ deg}) = 70$ μm . The initiation of blade oscillations and the sudden increase of the coating profile are also concomitant, in the vicinity of the second contact location where the cylinder coating profile reached a maximum $w(\Phi = 290 \text{ deg}) = 62$ μm . This outline is maintained until approximately $\Phi = 300$ deg, where it drops again to a lower value range $w = [42; 60]$ μm . The blade dynamics are then disrupted once again by the occurrence of an abradable coating profile peak $w(\Phi = 52 \text{ deg}) = 63$ μm and a smaller blade bending displacement (D_T) than encountered before (Revolution 3, orange curve). These interactions take place at the same location in the third and fourth revolutions, along with the gradual increase of the blade tip oscillation amplitude. Furthermore, it can be noted in Fig. 8(a), upper graph, that three distinct lobes

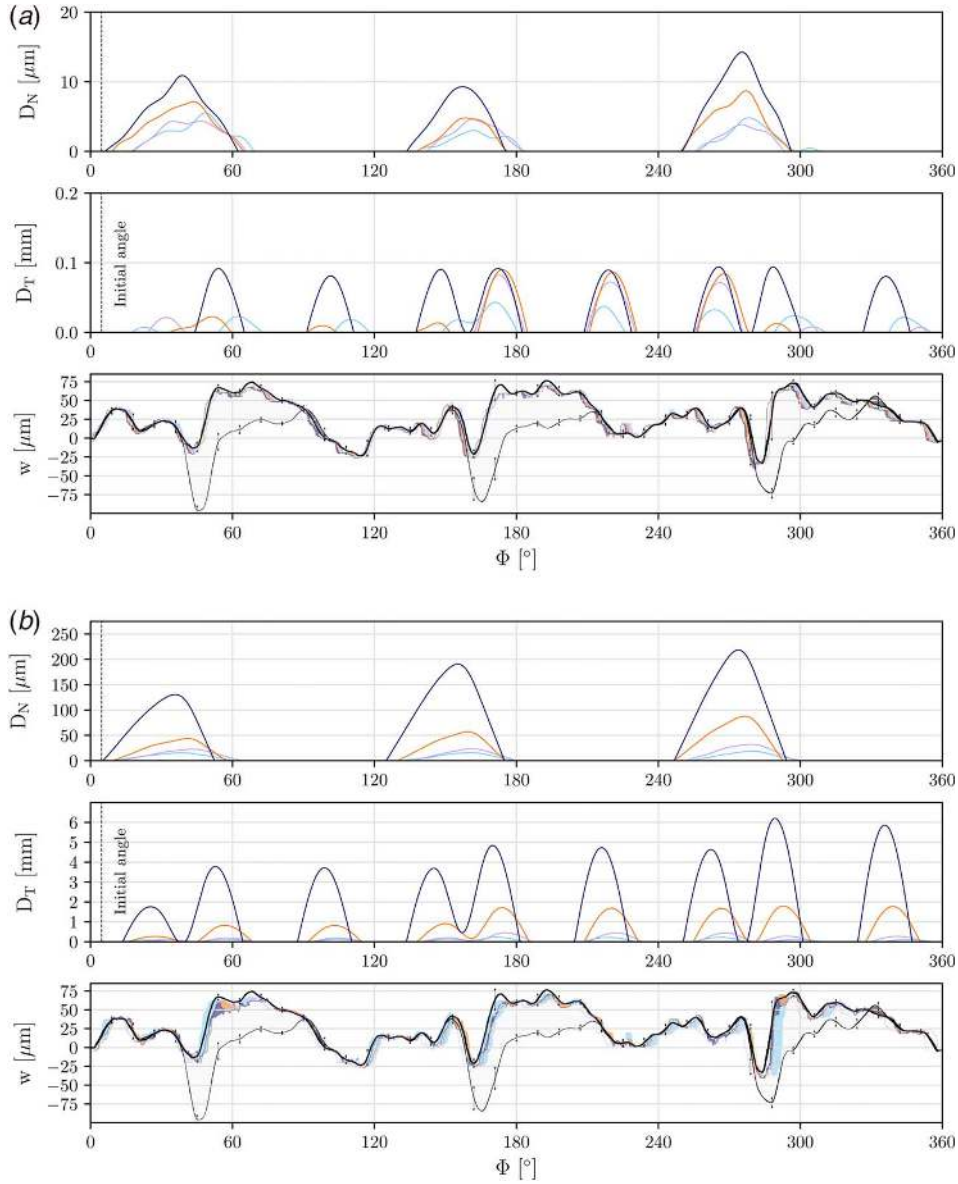


Fig. 8 Blade-coating rubs diagrams of experiment 2 in (a) phase 1 and (b) phase 2. **Note 1:** Colors correspond to cylinder revolution: Revolution 1 (–), 2 (–), 3 (–), and 4 (–). **Note 2:** Three embedded diagrams are plotted according to the coating angular position Φ : blade foot horizontal displacement D_N , blade bending vertical displacement D_T , and coating profile w and coating loss.

start to take shape in the incursion cell horizontal motion, with each lobe coinciding with one of the previously identified contact locations. These considerations seem to corroborate the notion of blade divergence originating from a synchronization mechanism between the blade motion and the abradable coating pattern.

Phase 2. The investigations of the blade-coating interactions are continued in Phase 2 over four revolutions, as depicted in Fig. 8(b). The creation of a three-lobe pattern is maintained for the incursion cell displacement (D_N) along with a nine-lobe pattern for the blade vertical oscillation (D_T). To be specific, this last pattern derives from the repetition, at the three contact locations $\Phi = 50, 172, 285$ deg, of the following sequence of events: (I) the blade completes one full oscillation; (II) it initiates a second oscillation, but the coincidence of blade descent and incursion cell translation movement generates a contact; (III) the blade is instantaneously pushed upward out of contact and starts a new oscillation. The two bonded lobes, indicating the contact location, are assigned to stages (II) and (III), whereas the separated lobe is related to stage

(I). This pattern promotes repetitive rubs at the same coating angular position (Φ) at every revolution and therefore tends to increase the blade vertical amplitude from $D_T = 0.1$ mm in revolution 1 (–) to $D_T = 6.3$ mm in revolution 4 (–). As the blade undergoes a greater oscillation amplitude, the amount of potential energy stored gets larger, which consequently induces harder rubs with the abradable coating. Indeed, nonnegligible wear can be observed in the surroundings of the coating profile peaks and allocated to contacts occurring in the third and the fourth revolutions. The incursion cell apparent incursion (D_N) also reveals the intensity of contacts via the displacement amplitude, which is substantially increased from $D_N = 17$ μm in revolution 1 (–) to $D_N = 220$ μm in revolution 4 (–).

Phase 3. Both of the vertical and horizontal displacements of interest experienced their maximum amplitude in this phase. The interaction diagram plotted in Fig. 9(a) highlights the fact that the blade vertical position reached $D_T = 8.3$ mm at $\Phi^{(\text{Rev}3)} = 171$ deg and the incursion cell, $D_N = 300$ μm at $\Phi^{(\text{Rev}3)} = 35$ deg. Moreover,

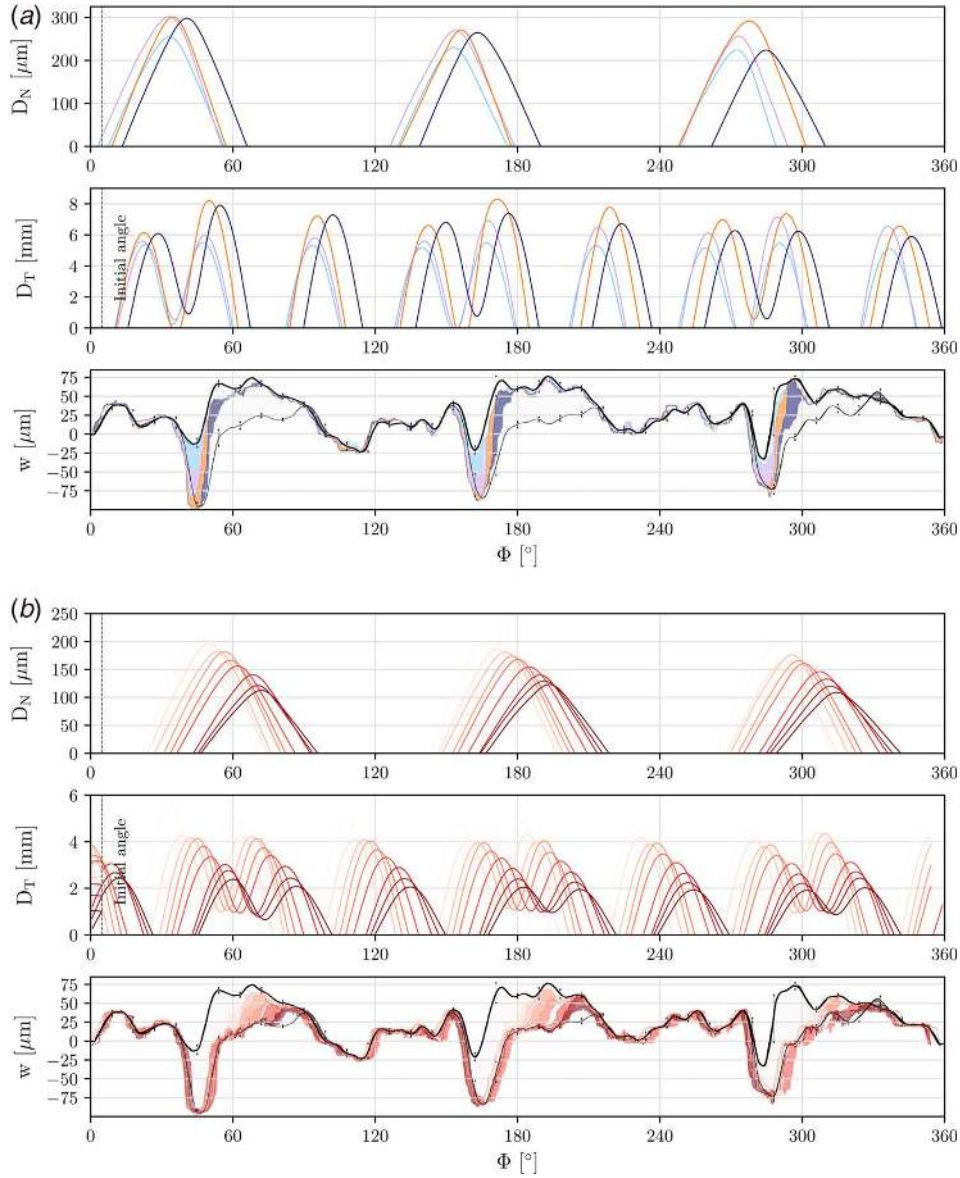


Fig. 9 Blade-coating rubs diagrams of experiment 2 in (a) phase 3 and (b) phase 4. **Note 1:** Colors are set to cylinder revolution: (a) Revolution 1 (–), 2 (–), 3 (–), and 4 (–); (b) from revolution 1 (–) to 9 (–). **Note 2:** Three embedded diagrams are plotted according to the coating angular position Φ : blade foot horizontal displacement D_N ; blade bending vertical displacement D_T ; and coating profile w and coating loss.

significant rub-induced wear shows up on the diagram, at the three contact location $\Phi = 50, 172, 285$ deg, revealing that almost $100 \mu\text{m}$ of abradable coating was scoured out during the first two revolutions. As the abradable coating was removed, the contact occurrence was delayed, and the location slightly shifted toward the positive coating angular position (Φ). Thus, in the third and fourth revolutions, it keeps moving to the right, as do the three-lobe pattern of the incursion cell (D_N) and the nine-lobe pattern of the blade (D_T). The peaks of the coating profile, which initiated the oscillations, have been removed and the coating profile has been flattened at these locations, but there remains a huge amount of energy stored in the blade-incursion cell vibrational system remains huge at the end of the second revolution. The incursion cell motion continues with a $200 \mu\text{m}$ amplitude pace in the third and fourth revolutions, which sustain the occurrence of contacts and the synchronization mechanism.

Phase 4. After reaching the peak amplitude in phase 3, both the vertical and horizontal components of the blade displacement enter

a decreasing stage. The present phase consists of the final nine revolutions of interest of experiment 2. These are depicted in the interaction diagram of Fig. 9(b) with a different color code than used before to identify a revolution: it changes linearly, from light red to dark red. The shifting process of the contact location discussed in phase 3 is definitely continued in these revolutions. On the one hand, the incursion cell and blade bending motion are slowly damped by blade-coating interactions: the accommodation of contact and the ejection of wear debris tend to dissipate the kinetic energy of impact and therefore the amount of energy stored in the blade. On the other hand, the repetitive rubbing has removed coating from the contact location, which simply aborts the possibility of any further occurrence of interaction.

4 Synchronization Mechanisms

The investigations conducted in experiments 1 and 2 have highlighted two mechanisms, which account for the repetition of

blade–coating interactions at a specific rate: (i) a blade–incursion cell synchronization based on their respective natural frequencies and (ii) an incursion cell–coating profile synchronization generated from the excitation of the incursion cell by the abradable coating pattern.

Blade–Incursion Cell. From the consideration of both blade and incursion cell natural frequencies, we observed that every oscillation of the incursion cell on the horizontal axis is associated with n_k oscillations of the blade on the vertical axis ($n_k \approx 2.8$). Since the number n_k is not an integer, these signals are not always synchronized. They return to their initial respective values after N cycles have been completed. This is what we have called here the blade–incursion cell synchronization pattern.

To depict this mechanism, we have chosen to consider two signals, written hereafter as signal A and signal B, assimilated to the incursion cell displacement (D_N) and the blade bending displacement (D_T) at the frequencies $f_A = 150$ Hz and $f_B = 425$ Hz. Both signals are sinusoidal, without damping, and the amplitude set to unity. The phase shift between the two signals is set to $\varphi = 79.5$ deg to have a perfect overlap between the curves, but any other value would give a similar pattern. The synchronization–desynchronization between the two signals is indicated using a third signal, written signal C, whereby signal C = signal A + signal B. The time–evolution of these signals is presented in Fig. 10(a) as well as the different states of synchronization between signal A and signal B, identified by the following symbols: E^+ , B^+ , B^- , E^- , A^- , A^+ . The state E^+ , consists of perfect synchronization: signals A and B are in-phase. This is demonstrated by the amplitude of signal C, which is twice the unity. This state is reached every $N=6$ cycles for signal A and $N.n_k$ cycles for signal B. Reciprocally, state E^- , is

assigned to the situation, where signal B is in phase opposition with signal A. The other states (B^+ , B^- , A^- , A^+), are intermediate states between E^+ , and E^- , and are detailed in Fig. 10(b).

The six states of synchronization are equivalent to modes of the blade–incursion cell vibrational system in which a rub event is more likely; hence, we presume the incursion cell displacement (D_N) to be maximum and the blade bending displacement (D_T) to take one of six main configurations. As previously mentioned, the state E^+ , is the configuration in which the two signals are in-phase; the incursion cell is fully translated, but the blade tip is at the upper position. We call this state “Evasive Up” because the blade is escaping from the cylinder. The state E^- , is symmetrical to this one and is called “Evasive Down,” where the blade tip is at the lowest position. Then, we have states A^+ , and B^+ , when the blade tip is positive in the configuration of B-coupling and A-coupling and their symmetrical states A^- , and B^- , when the blade tip is negative. These couplings have been mentioned in the works of Millecamps et al. [13] and Mandard et al. [27] and refer to the direction of the blade velocity vector just before impact: A-coupling if blade velocity direction is opposite to the direction of cylinder tangential velocity and B-coupling if blade velocity direction is identical to the direction of cylinder tangential velocity. It is assumed that A-coupling tends to damp blade oscillation, whereas B-coupling amplifies it.

The analysis of blade–coating interactions reveals that only B-coupling (Up and Down) occurred in experiment 1, whereas only A-coupling Up are found in experiment 2 (except A-coupling Down in phase 2 at $\Phi^{(Rev4)} = 275$, deg). It corroborates our initial assumption regarding the origin of two distinct mechanisms: in experiment 1, only the incursion cell kinematics drives the

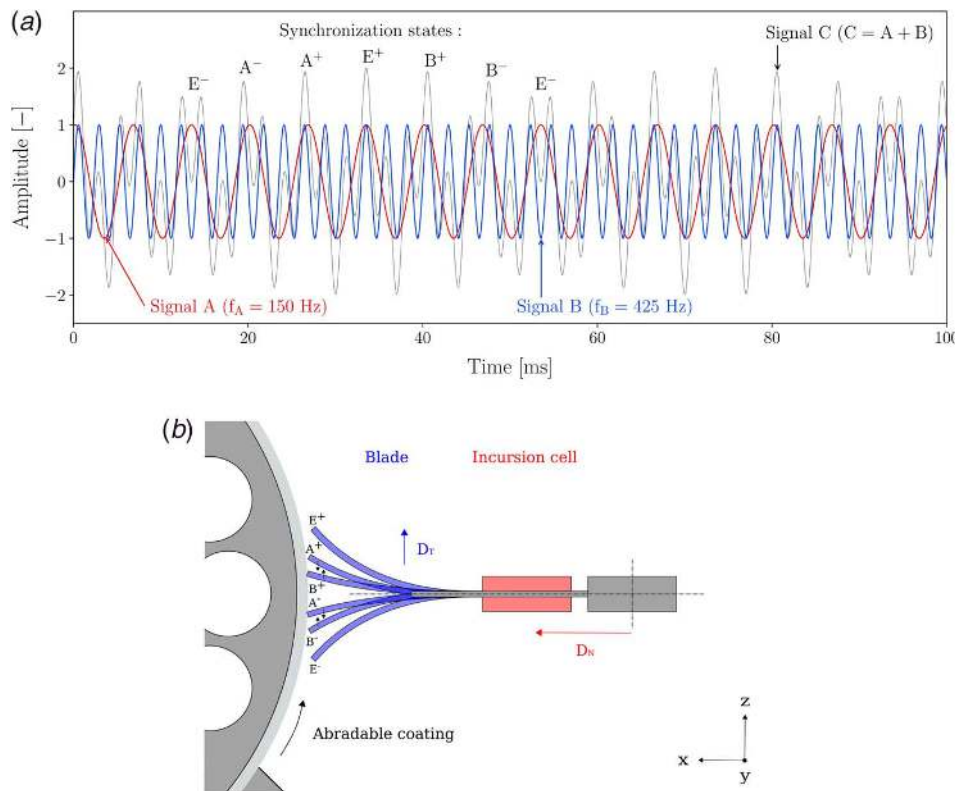


Fig. 10 Blade-incursion cell synchronization mechanism assuming theoretical oscillations signals (D_N , D_T) in (a) and the associated synchronization states in (b). Note 1: Signals A and B are, respectively, the theoretical oscillations of incursion cell (D_N) and blade (D_T) without any consideration of damping. Note 2: Synchronization states are defined by parameters $\{D_N, D_T, d(D_T)/dt\}$ and listed: E^+ , evasive up $\{1, +1, 0\}$; B^+ , B-coupling up $\{1, +0.49, +0.87\}$; B^- , B-coupling down $\{1, -0.50, +0.86\}$; E^- , evasive down $\{1, -1, 0\}$; A^- , A-coupling down $\{1, -0.49, -0.87\}$; A^+ , A-coupling up $\{1, +0.50, -0.86\}$.

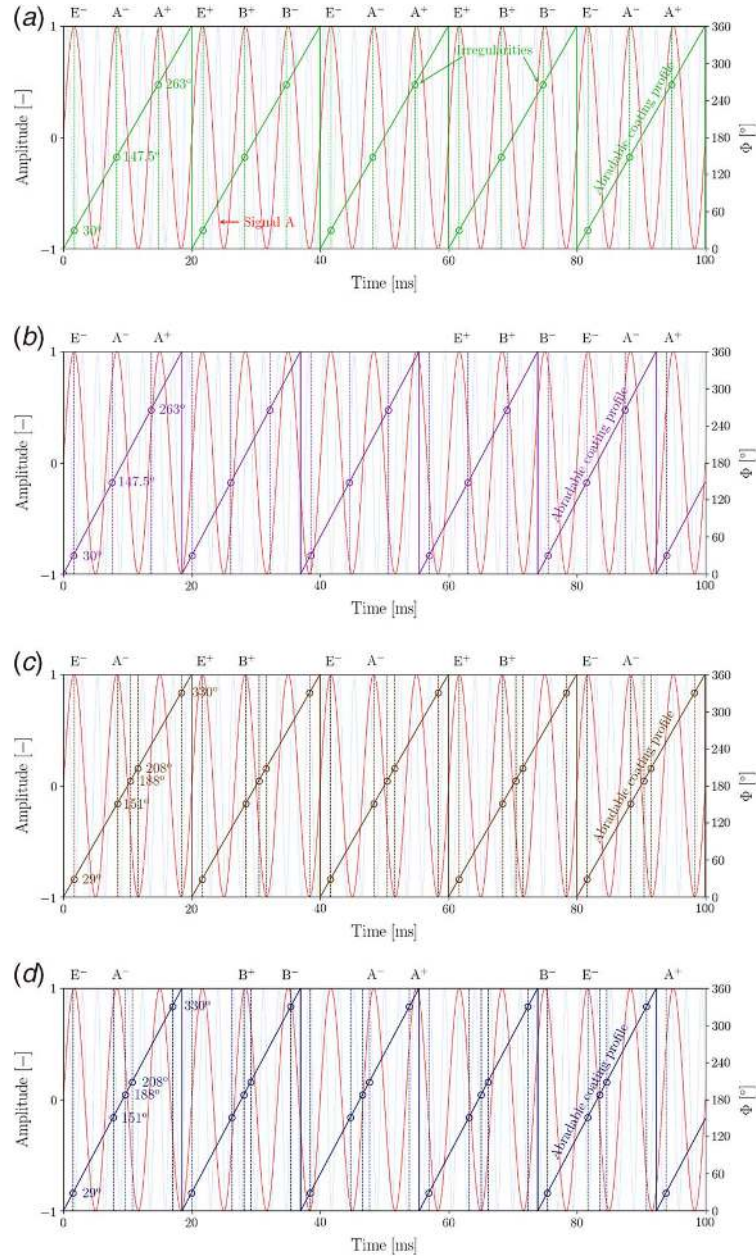


Fig. 11 Incursion cell–coating profile synchronization mechanism with various coating profile patterns and blade–coating velocities. Note: Symbols E^+ , B^+ , B^- , E^- , A^- , A^+ refer to blade–coating couplings presented in Fig. 10.

contact, along with the subsequent blade vibration, which is facilitated by the B-coupling configuration, whereas in experiment 2, contact is initiated by coating profile irregularities, under a forced A-coupling configuration, but sustained by the combination of both synchronization mechanisms (blade–incursion cell and incursion cell–coating profile).

Incursion Cell–Coating Profile. The main feature of this synchronization mechanism lies in the compliance of the incursion cell oscillations and the coating profile irregularities. First, the relative blade–coating velocity V_T should be such that the number of incursion cell oscillations per revolution (k_x) is an integer. Second, the oscillation should reach its peak value when a coating profile irregularity is close to the blade tip contact area.

To depict this mechanism, signals A and B introduced before are used with a phase set to $\varphi = 0$ deg to get three distinct peaks of signal A per cylinder revolution. The blade–incursion cell couplings E^+ ,

B^+ , B^- , E^- , A^- , A^+ , presented in Fig. 10 are still valid, but contact occurrence also depends on the coating profile pattern and the relative blade–coating velocity V_T . Four configurations pictured in Fig. 11 have been selected to highlight the possibilities of interaction:

- (1) Cylinder velocity is set to $V_T = 46.2$ m/s to get an integer number of oscillations per revolution $k_x = 3$, and coating irregularities are periodically set on the cylinder to $\Phi = 30$ deg, 147.5 deg, 263 deg.
- (2) Cylinder velocity is set to $V_T = 50$ m/s, a noninteger number of oscillations per revolution $k_x = 2.7$ and an identical coating profile configuration to (a).
- (3) Cylinder velocity is set to $V_T = 46.2$ m/s ($k_x = 3$) and coating irregularities are randomly set on the cylinder to $\Phi = 29$ deg, 151 deg, 188 deg, 208 deg, 330 deg.

- (4) Cylinder velocity is set to $V_T = 50$ m/s ($k_x = 2.7$) and an identical coating profile configuration as (c).

In the configuration of Fig. 11(a), a perfect synchronization is exhibited between coating irregularities and incursion cell oscillations. Blade–coating contacts are inevitable: even if the blade escapes contact in the uppermost position, under E^+ -coupling, at a given time, it will be followed by A^+ , and A^- , coupling in the next cycles, which makes contact occurrence with the coating irregularities even more likely. Reciprocally, an appropriate phase shift initially set between signal A and the irregularities would have made contacts almost impossible to occur. In the configuration of Fig. 11(b), cylinder velocity is slightly changed. A noninteger k_x -value implies that the peak value of signal A cannot be associated with a given coating angular position Φ . In other words, the contact location changes throughout the revolutions, and the blade never encounters the same part of the cylinder. Despite a coating profile with periodic irregularities, the occurrence of a synchronization mechanism seems very unlikely under these circumstances. A random set of coating profile irregularities is investigated in Fig. 11(c) with a cylinder velocity such that the k_x -value is an integer. Some irregularities might match oscillation peaks, which therefore makes the initiation of a synchronization mechanism highly probable. The last configuration pictured in Fig. 11(d) makes the occurrence of synchronization very unlikely because contacts do not involve the same coating location from one revolution to the next, and the distribution of irregularities is random.

These four configurations give an overview of the unlikelihood of incursion cell–coating profile coupling occurrence: the probability of contact occurrence depends on the coincidence of blade motion under vibration and the rate of coating irregularities. The better the blade oscillation pattern matches the rate of coating irregularities, the more likely is the occurrence of a divergence. However, it should be noted that, after hard contact, the blade might be induced into a larger amplitude of motion than expected, then setting a subsequent phase shift between the blade vibration and the rate of coating irregularities. Therefore, this mechanism tends to abort the divergent behavior after an intense rub event. As a consequence, the blade divergence appears as a most unlikely and unstable state of motion, since it combines the coincidence of blade and incursion cell vibration (which can be avoided by mistuning frequencies of the blade, casing and bladed-disk), an appropriate rotation velocity for the coating defects to meet the blade tip at every revolution, and a series of low-intensity impacts, which sustain the coupling but avoid the setting of a phase shift between the coating irregularities and the blade.

5 Conclusions

In this article, two experiments on blade–abradable coating interactions were performed on a special setup, with a high-frequency data acquisition system and a fully instrumented flat blade, and were used to capture the dynamics of rub events. Blade vertical bending (D_T), blade foot horizontal translation movement (D_N), and coating profile (w) were tracked throughout the tests to identify the mechanisms responsible for the amplification of blade vibrations. These investigations were conducted using a three-embedded interaction diagram, which compares, on the same time-line, the blade vertical and horizontal displacements and the current abradable coating profile in the vicinity of the rub location. It enabled the rewriting of the sequence of events, which initiated and sustained the blade divergence observed in both experiments 1 and 2. The following conclusions can therefore be drawn:

- The first natural frequencies of the blade vertical bending and incursion cell translation movement (i.e., blade foot apparent incursion) are, respectively, $T_z^1 = 425$ Hz and $B_x^1 = 150$ ($n_k = B_z^1/T_x^1 \approx 2.8$). The vibrations are almost synchronized with 2.8 vertical oscillations for every horizontal one. This implies a synchronization pattern, described in Fig. 10, in

which the relative position of the blade and the incursion cell takes six different states (E^+ , B^+ , B^- , E^- , A^- , A^+); before reverting to the initial state. We have called this the blade–incursion cell synchronization mechanism. In a full-scale turbofan, this would be equivalent, assuming negligible vibration of the casing, to the synchronization of the bladed-disk radial motion with the blade bending or twisting motion.

- A blade–coating interaction is enabled when the conditions of “contact occurrence” are satisfied: blade foot translation is maximum and blade bending is minimum (when the blade lies on the horizontal axis).
- After actuation ended and a first contact initiated in experiment 1, both horizontal and vertical motions turned into free oscillations with a phase shift accidentally set to fit the conditions of “contact occurrence.” Height B-coupling rubs followed, with an increasing blade amplitude, and stopped when a new state of synchronization E^+ , was reached (the blade foot fully displaced toward the abradable coating track but the blade avoiding contact).
- Rubs can be twofold: either the blade is moved toward the coating or the coating is brought toward the blade. Although it seemed unlikely, the second case was observed in experiment 2 with a periodic pattern of three irregularities observed on the abradable coating cylinder. This initiated the horizontal and vertical motion of the blade and produced three preferential contact locations $\Phi = 50$ deg, 172 deg, 285 deg. We have called this phenomenon the incursion cell–coating profile synchronization mechanism, and it occurs when the blade–coating interaction is repeated at every revolution on the same coating profile irregularity (see Fig. 11). An equivalent mechanism could be found in a full-scale turbofan in situations, where wear lobes, ovalization, and heat expansion of the casing promotes an angular pattern of irregularities, which can regularly meet a blade.
- The combination of the two synchronization mechanisms generated the divergent behavior of the blade in experiment 2. The vibrations are damped as soon the abradable coating irregularities are removed by repetitive rubs and the excitation source is cancelled out.

Acknowledgment

Financial support for this study is gratefully acknowledged from the following sources: Safran Aircraft Engine (SNECMA), the French National Association for Research-based Technology (ANRT), and the ELSAT2020 project, which is co-financed by the European Union with the European Regional Development Fund, the French State, and the Hauts-de-France Regional Council. The authors would also like to extend their special thanks to Romain Mandard, who conducted these experiments during his PhD thesis and provided a relevant review of this article.

Conflict of Interest

There are no conflicts of interest.

References

- [1] Benini, E., 2004, “Three-Dimensional Multi-Objective Design Optimization of a Transonic Compressor Rotor,” *J. Propul. Power.*, **20**(3), pp. 559–565.
- [2] Srinivasan, A. V., 1997, “Flutter and Resonant Vibration Characteristics of Engine Blades,” *ASME J. Eng. Gas Turbines Power.*, **119**(4), pp. 742–775.
- [3] Yu, P., Zhang, D., Ma, Y., and Hong, J., 2018, “Dynamic Modeling and Vibration Characteristics Analysis of the Aero-Engine Dual-Rotor System With Fan Blade Out,” *Mech. Syst. Signal. Process.*, **106**, pp. 158–175.
- [4] Carter, T. J., 2005, “Common Failures in Gas Turbine Blades,” *Eng. Failure Anal.*, **12**(2), pp. 237–247.
- [5] Silveira, E., Atxaga, G., and Irisarri, A., 2008, “Failure Analysis of a Set of Compressor Blades,” *Eng. Failure Anal.*, **15**(6), pp. 666–674.
- [6] Lourenço, N., Graça, M., Franco, L., and Silva, O., 2008, “Fatigue Failure of a Compressor Blade,” *Eng. Failure Anal.*, **15**(8), pp. 1150–1154.

- [7] Poursaeidi, E., Babaei, A., Arhani, M. M., and Arablu, M., 2012, "Effects of Natural Frequencies on the Failure of R1 Compressor Blades," *Eng. Failure Anal.*, **25**, pp. 304–315.
- [8] Witek, L., Wierzbńska, M., and Poznańska, A., 2009, "Fracture Analysis of Compressor Blade of a Helicopter Engine," *Eng. Failure Anal.*, **16**(5), pp. 1616–1622.
- [9] Ma, H., Yin, F., Guo, Y., Tai, X., and Wen, B., 2016, "A Review on Dynamic Characteristics of Blade–Casing Rubbing," *Nonlinear Dynam.*, **84**(2), pp. 437–472.
- [10] Jacquet-Richardet, G., Torkhani, M., Cartraud, P., Thouverez, F., Gibert, C., Baguet, S., Almeida, P., and Peletan, L., 2013, "Rotor to Stator Contacts in Turbomachines. Review and Application," *Mech. Syst. Signal. Process.*, **40**(2), pp. 401–420.
- [11] Millecamps, A., 2010, "Interaction Aube-carter: Contribution De L'usure De L'abradable Et De La Thermomécanique Sur La Dynamique D'aube," PhD thesis, Université de Lille 1, France.
- [12] Padova, C., Barton, J., Dunn, M. G., and Manwaring, S., 2006, "Experimental Results From Controlled Blade Tip/Shroud Rubs at Engine Speed," *ASME J. Turbomach.*, **129**(4), pp. 713–723.
- [13] Millecamps, A., Brunel, J.-F., Garcin, F., and Nucci, M., 2009, "Influence of Thermal Effects During Blade-Casing Contact Experiments," *ASME 2009 International Design Engineering Technical Conferences and Computers and Information in Engineering Conference*, San Diego, CA, Aug. 30–Sept. 2, pp. 855–862.
- [14] Legrand, M., Batailly, A., and Pierre, C., 2011, "Numerical Investigation of Abradable Coating Removal in Aircraft Engines Through Plastic Constitutive Law," *ASME J. Comput. Nonlinear. Dyn.*, **7**(1), p. 011010.
- [15] Williams, R. J., 2011, "Simulation of Blade Casing Interaction Phenomena in Gas Turbines Resulting From Heavy Tip Rubs Using an Implicit Time Marching Method," *ASME 2011 Turbo Expo: Turbine Technical Conference and Exposition*, Vancouver, British Columbia, Canada, June 6–10, pp. 1007–1016.
- [16] Sinha, S. K., 2005, "Non-linear Dynamic Response of a Rotating Radial Timoshenko Beam With Periodic Pulse Loading at the Free-End," *Int. J. Non-Linear Mech.*, **40**(1), pp. 113–149.
- [17] Schmiechen, P., 1997, "Travelling Wave Speed Coincidence," PhD thesis, Imperial College London (University of London), UK
- [18] Legrand, M., Pierre, C., Cartraud, P., and Lombard, J.-P., 2009, "Two-Dimensional Modeling of an Aircraft Engine Structural Bladed Disk-Casing Modal Interaction," *J. Sound. Vib.*, **319**(1–2), pp. 366–391.
- [19] Batailly, A., Legrand, M., Millecamps, A., and Garcin, F., 2015, "Conjectural Bifurcation Analysis of the Contact-Induced Vibratory Response of an Aircraft Engine Blade," *J. Sound. Vib.*, **348**, pp. 239–262.
- [20] Baiz, S., Fabis, J., Boidin, X., and Desplanques, Y., 2013, "Experimental Investigation of the Blade/Seal Interaction," *Proc. Inst. Mech. Eng., Part J: J. Eng. Tribology*, **227**(9), pp. 980–995.
- [21] Mandard, R., Witz, J.-F., Boidin, X., Fabis, J., Desplanques, Y., and Meriaux, J., 2015, "Interacting Force Estimation During Blade/Seal Rubs," *Tribol. Int.*, **82**(Part B), pp. 504–513.
- [22] Mandard, R., Desplanques, Y., Hauss, G., Fabis, J., Witz, J.-F., and Meriaux, J., 2015, "Mechanisms of Incursion Accommodation During Interaction Between a Vibrating Blade and an Abradable Coating," *Wear*, **330–331**, pp. 406–418.
- [23] Almeida, P., Gibert, C., Thouverez, F., Leblanc, X., and Ousty, J.-P., 2014, "Experimental Analysis of Dynamic Interaction Between a Centrifugal Compressor and Its Casing," *ASME J. Turbomach.*, **137**(3), p. 031008.
- [24] Batailly, A., Agrapart, Q., Millecamps, A., and Brunel, J.-F., 2016, "Experimental and Numerical Simulation of a Rotor/Stator Interaction Event Localized on a Single Blade Within an Industrial High-Pressure Compressor," *J. Sound. Vib.*, **375**, pp. 308–331.
- [25] Kou, H.-J., Lin, J.-S., Zhang, J.-H., and Fu, X., 2017, "Dynamic and Fatigue Compressor Blade Characteristics During Fluid-Structure Interaction: Part I-Blade Modelling and Vibration Analysis," *Eng. Failure Anal.*, **76**, pp. 80–98.
- [26] Piollet, E., Nyssen, F., and Batailly, A., 2019, "Blade/Casing Rubbing Interactions in Aircraft Engines: Numerical Benchmark and Design Guidelines Based on Nasa Rotor 37," *J. Sound. Vib.*, **460**, p. 114878.
- [27] Mandard, R., Witz, J.-F., Desplanques, Y., Fabis, J., and Meriaux, J., 2014, "Wavelet Analysis of Experimental Blade Vibrations During Interaction With an Abradable Coating," *ASME J. Tribol.*, **136**(3), p. 031102.